Computational Geosciences (2021) 25:775–792
https://doi.org/10.1007/s10596-020-09964-3

ORIGINAL PAPER

A macroelement stabilization for mixed finite element/finite volume discretizations of multiphase poromechanics

Julia T. Camargo[1] · Joshua A. White[2] · Ronaldo I. Borja[1]

Received: 27 June 2019 / Accepted: 1 April 2020 / Published online: 18 June 2020

Abstract

Strong coupling between geomechanical deformation and multiphase fluid flow appears in a variety of geoscience applications. A common discretization strategy for these problems is a continuous Galerkin finite element scheme for the momentum balance equation and a finite volume scheme for the mass balance equations. When applied within a fully implicit solution strategy, however, this discretization is not intrinsically stable. In the limit of small time steps or low permeabilities, spurious oscillations in the piecewise-constant pressure field, i.e., checkerboarding, may be observed. Further, eigenvalues associated with the spurious modes will control the conditioning of the matrices and can dramatically degrade the convergence rate of iterative linear solvers. Here, we propose a stabilization technique in which the mass balance equations are supplemented with stabilizing flux terms on a macroelement basis. The additional stabilization terms are dependent on a stabilization parameter. We identify an optimal value for this parameter using an analysis of the eigenvalue distribution of the macroelement Schur complement matrix. The resulting method is simple to implement and preserves the underlying sparsity pattern of the original discretization. Another appealing feature of the method is that mass is exactly conserved on macroelements, despite the addition of artificial fluxes. The efficacy of the proposed technique is demonstrated with several numerical examples.

Keywords Poroelasticity · Reservoir simulation · Inf-sup stability · Finite element method · Finite volume method

1 Introduction

In a variety of applications, it is useful to model the hydromechanical behavior of porous media infiltrated by one or more fluids—e.g., in geotechnical engineering [1–20], hydrocarbon recovery [21–30], and geologic carbon storage [31–33]. Precise models should account for the tight interaction between solid deformation and fluid flow. The conceptual framework for modeling this coupled behavior is well established [34, 35], with Biot's work [36] providing a sound theoretical foundation. Computational methods for poromechanics, however, still pose many interesting challenges. In particular, this work focuses on numerical instabilities that may arise due to the discretization spaces chosen for the coupled fields.

As a representative problem, we consider a model in which an elastic solid skeleton is saturated with two immiscible fluids. We present the multiphase formulation for its relevance in many geoscience applications, though the single-phase formulation is a straightforward subcase. The behavior of the porous system is governed by a momentum balance equation for the mixture and mass balance equations for each of the fluids. A fully implicit time integration strategy is adopted, where all unknown fields are updated simultaneously in a monolithic manner [37, 38]. A variety of finite element and finite volume–based discretization strategies may be applied to these equations, each with their own advantages [39–54]. Of specific interest here is a frequent choice: continuous trilinear interpolation for the displacement unknowns and element-wise constant fields for the pressure and saturation

✉ Julia T. Camargo
jcamargo@stanford.edu

Joshua A. White
jawhite@llnl.gov

Ronaldo I. Borja
borja@stanford.edu

[1] Department of Civil and Environmental Engineering, Stanford University, Stanford, CA, USA

[2] Atmospheric, Earth and Energy Division, Lawrence Livermore National Laboratory, Livermore, CA, USA

unknowns. Such an interpolation results, for example, when applying a continuous Galerkin finite element scheme to the momentum balance equation, and a finite volume scheme to the mass balance equations [38, 40, 44, 46].

This discretization works well in a variety of practical cases. The chosen interpolation spaces, however, can be problematic. In the limit of small time steps or low permeabilities, undrained deformation can occur. The fluid mass balance equations impose an incompressibility constraint on the deformation field. Like many other constrained problems—e.g., Stokes flow, incompressible elasticity, or contact problems [55]—these divergence constraints can create numerical instabilities if the discrete approximations for the field variables do not satisfy the Ladyzhenskaya-Babuška-Brezzi (LBB or inf-sup) condition [56, 57]. Unfortunately, the combination explored here is not intrinsically LBB-stable. As a result, spurious oscillations, i.e., checkerboarding, may be observed in the pressure field. A less obvious, but equally important, symptom is a degradation in the convergence rate of iterative linear solvers. Near-zero eigenvalues associated with spurious modes will control the conditioning of the system matrices, leading to poorly conditioned systems and increased iteration counts. This latter issue can persist in regimes where checkerboarding is not visually apparent, and may thus go unnoticed by practitioners.

These instabilities may be treated with a carefully designed perturbation to the constraint equations. The goal is to remove instabilities while maintaining an accurate approximation of the underlying PDEs. This is the basic rationale behind many stabilization techniques, including the Brezzi and Pitkäranta scheme [58], the Galerkin Least-Squares approach [59], and the polynomial pressure projection technique [60]. Various stabilization schemes have been proposed that devote particular attention to constant pressure elements [61–65], starting with early work in [66]. In [64], the idea of penalizing the pressure jump across inter-elements boundaries was introduced. An important modification of this method, the local pressure jump (LPJ) stabilization, was developed in [65] based on the macroelement concept. These schemes were primarily developed for fluid mechanics problems. Since then, many stabilization schemes have been successfully applied to poromechanics with single-phase flow [52, 67–73]. However, the study of stabilization procedures addressing multiphase problems is still incipient, with just a few studies available [74, 75].

This paper proposes a new stabilization technique in which the mass balance equations are supplemented with stabilizing flux terms. The resulting technique mimics the LPJ stabilization [65, 76, 77] in its basic design, but with suitable extensions to handle the multiphase and poromechanical system of interest here. The additional stabilization terms are dependent on a stabilization parameter that must be well chosen to suppress instabilities while not compromising solution accuracy. We identify an optimal value for this parameter using an analysis of the eigenvalue distribution of the macroelement Schur complement matrix. The resulting method is simple to implement and preserves the underlying sparsity pattern of the original discretization. Another appealing feature of the method is that mass is exactly conserved on macroelements.

We remark that the goal of this work is to "fix" a widely used discretization technique, but it is certainly not the only pathway to stable solutions. For example, significant work has been invested over the years on finding intrinsically inf-sup stable interpolation spaces—e.g., [39, 49, 51, 78]. Alternatively, another viable strategy is to avoid the monolithic system altogether, and rather solve the coupled PDEs in a partitioned way using a sequential implicit approach [40, 44, 47]. In this case, no saddle-point structure will ever appear. Unfortunately, the convergence rate and clock time of a sequential scheme is generally worse than a well-designed monolithic scheme [37]. To exploit efficient and scalable monolithic solvers [38, 79, 80], we therefore prefer to address the stability problem head on.

The paper is organized as follows. The governing equations and discretization scheme are introduced in Sections 2 and 3. In Section 4, we examine the behavior of this model in the undrained limit, in order to identify the source of spurious modes. To fix this deficiency, our stabilization scheme is detailed in Section 5. The resulting approach both treats spurious pore pressure oscillations and improves the conditioning of the system matrices. This is demonstrated through numerical examples presented in Section 6. Finally, concluding remarks are given in Section 7.

2 Governing equations

We consider a multiphase poroelastic problem in which two immiscible fluids fill the voids of the porous, deformable solid skeleton. We focus on a displacement-saturation-pressure formulation, ignoring dynamic and non-isothermal effects. We further neglect capillary forces, meaning, the wetting and non-wetting fluid phases have equal pressure inside the pore. This simplification is common in many reservoir-scale simulations [81] and, in fact, the inclusion of capillarity would not change the stabilization scheme derived here.

The porous medium occupies a domain $\Omega \in \mathbb{R}^3$ over time interval $\mathcal{I} = (0, T]$. The unknown fields are the displacement of the solid $\mathbf{u} : \Omega \times \mathcal{I} \to \mathbb{R}^3$, the wetting fluid saturation $s : \Omega \times \mathcal{I} \to \mathbb{R}$, and the fluid pressure

$p : \Omega \times \mathcal{I} \to \mathbb{R}$. The initial/boundary value problem is governed by a linear momentum balance for the mixture and two mass balance equations for the wetting (w) and non-wetting (o) fluids, respectively:

$$\nabla \cdot \boldsymbol{\sigma}' - b\nabla p + \rho \mathbf{g} = \mathbf{0} \qquad \text{in } \Omega \times \mathcal{I}, \tag{1a}$$

$$\dot{m}_w + \nabla \cdot \mathbf{w}_w - q_w = 0 \qquad \text{in } \Omega \times \mathcal{I}, \tag{1b}$$

$$\dot{m}_o + \nabla \cdot \mathbf{w}_o - q_o = 0 \qquad \text{in } \Omega \times \mathcal{I}. \tag{1c}$$

In Eq. 1a, the effective Cauchy stress depends on the symmetric gradient of the displacement field as

$$\boldsymbol{\sigma}' = \mathbb{C} : \nabla^s \mathbf{u}, \tag{2}$$

where $\mathbb{C}$ is the drained elasticity tensor. Biot's coefficient $b = 1 - K_{dr}/K_s$ may be calculated from K_{dr}, the drained skeleton bulk modulus, and K_s, the intrinsic bulk modulus of the solid phase. The mixture density ρ is related to the individual phase densities—denoted by ρ_ℓ for $\ell = \{w, o\}$ and ρ_s—via the relationship

$$\rho = (1 - \phi)\rho_s + \phi\rho_w s + \phi\rho_o(1 - s) \tag{3}$$

where ϕ is the porosity. Porosity changes are related to solid deformation and fluid pressure changes as

$$\dot{\phi} = b\nabla \cdot \dot{\boldsymbol{u}} + \frac{(b - \phi_0)(1 - b)}{K_{dr}}\dot{p}, \tag{4}$$

which introduces a coupling between the momentum and mass balance equations. Each fluid phase requires a density model $\rho_\ell(p)$, such as the simple linear model

$$\rho_\ell = \rho_\ell^0 \left[1 + \frac{1}{K_\ell}(p - p^0)\right] \tag{5}$$

with phase bulk modulus K_ℓ and reference density ρ_ℓ^0 at a reference pressure p^0.

In Eqs. 1b and 1c, m_ℓ is the mass per unit volume for the fluid phase $\ell = \{w, o\}$, with

$$m_w = \phi\rho_w s, \tag{6a}$$

$$m_o = \phi\rho_o(1 - s). \tag{6b}$$

The source terms q_ℓ are used to model well sources for injection and production of fluids, using a Peaceman well model [82, 83]. The mass flux $\mathbf{w}_\ell = (\rho_\ell \mathbf{v}_\ell)$ is linked to the pore pressure field via the generalized Darcy's law as

$$\mathbf{v}_\ell = -\lambda_\ell \boldsymbol{\kappa} \cdot \nabla(p + \rho_\ell g z). \tag{7}$$

The constitutive relation in Eq. 7 defines the volumetric flux $\mathbf{v}_\ell$ using the phase mobility $\lambda_\ell = k_{r\ell}/\mu_\ell$, the viscosity μ_ℓ, and the relative permeability $k_{r\ell}$. Specific relationships for viscosity $\mu_\ell = \mu_\ell(p)$ and relative permeability $k_{r\ell} = k_{r\ell}(s)$ must be defined for the fluids and porous medium under consideration. Additionally, $\boldsymbol{\kappa}$ represents the absolute permeability tensor, g the gravitational acceleration, and z the elevation above a datum.

The domain boundary Γ is decomposed into regions where Dirichlet and Neumann boundary conditions are specified, denoted by $\Gamma = \overline{\Gamma_{\mathbf{u}}^D \cup \Gamma_{\mathbf{u}}^N}$ for the momentum balance and $\Gamma = \overline{\Gamma_f^D \cup \Gamma_f^N}$ for the mass balances. These divisions follow the overlap restriction $\Gamma_{\mathbf{u}}^D \cap \Gamma_{\mathbf{u}}^N = \Gamma_f^D \cap \Gamma_f^N = \emptyset$. Specifically,

$$\mathbf{u} = \mathbf{0} \qquad \text{on } \Gamma_{\mathbf{u}}^D \times \mathcal{I}, \tag{8a}$$

$$\boldsymbol{\sigma} \cdot \mathbf{n} = \bar{\mathbf{t}} \qquad \text{on } \Gamma_{\mathbf{u}}^N \times \mathcal{I}, \tag{8b}$$

$$p = \bar{p} \qquad \text{on } \Gamma_f^D \times \mathcal{I}, \tag{8c}$$

$$s = \bar{s} \qquad \text{on } \Gamma_f^D \times \mathcal{I}, \tag{8d}$$

$$\mathbf{w}_w \cdot \mathbf{n} = 0 \qquad \text{on } \Gamma_f^N \times \mathcal{I}, \tag{8e}$$

$$\mathbf{w}_o \cdot \mathbf{n} = 0 \qquad \text{on } \Gamma_f^N \times \mathcal{I}, \tag{8f}$$

where the boundary conditions prescribing displacement (8a), total traction (8b), pore pressure (8c), wetting phase saturation (8d), wetting phase mass flux (8e), and non-wetting phase mass flux (8f) are given. Here, $\mathbf{n}$ denotes the outer normal vector. Homogeneous conditions on the displacement and external fluxes were chosen here to simplify some notations below, but these can be easily relaxed.

Initial conditions are specified as

$$\mathbf{u}(\mathbf{x}, 0) = \mathbf{u}_0(\mathbf{x}) \qquad (\mathbf{x}, t) \in (\Omega \times t = 0), \tag{9a}$$

$$s(\mathbf{x}, 0) = s_0(\mathbf{x}) \qquad (\mathbf{x}, t) \in (\Omega \times t = 0), \tag{9b}$$

$$p(\mathbf{x}, 0) = p_0(\mathbf{x}) \qquad (\mathbf{x}, t) \in (\Omega \times t = 0). \tag{9c}$$

Note that the single-phase poromechanics model arises as a subcase of these general equations if one fixes either $s(\mathbf{x}, t) = 0$ or $s(\mathbf{x}, t) = 1$. In this case, only one mass balance equation is required.

Clearly a number of modeling and constitutive assumptions are embedded in the formulation described above, but it remains a useful approximation for many subsurface applications. This formulation also contains many of the salient mathematical features that may be encountered in other models used in practice.

3 Discrete formulation

Figure 1 illustrates the basic geometry under consideration. The domain Ω is partitioned into a computational mesh $\mathcal{T}^h$ made of non-overlapping elements $\{K_i\}$ such that $\Omega = \bigcup_{i=1}^{n_e} K_i$. Every element face f is assigned a unique unit normal vector $\mathbf{n}_f$. For our stabilization procedure, we further assume that these elements may be

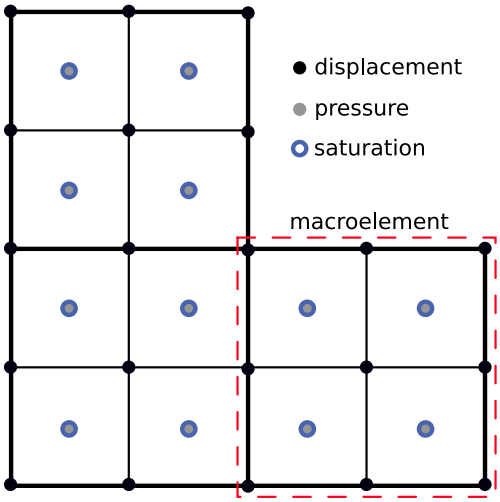

Fig. 1 Example mesh with nodal and cell-centered degrees-of-freedom. Each element is assigned to a parent macroelement

grouped into macroelements $\{M_i\}$ consisting of patches of eight hexahedra in 3D or four quadrilaterals in 2D. This configuration is readily achieved by beginning with a coarse version of the mesh and applying one level of structured refinement. We remark that for unstable elements, the effects of numerical instabilities are more pronounced for Cartesian grids and cubic elements [84, 85]. The extension of the basic method to fully unstructured grids is discussed later.

The discretization of the governing (1) is obtained using a mixed finite element/finite volume approach. An extensive description of this formulation is presented in [38]. Here, we briefly summarize the key components, but refer the interested reader there for a more complete exposition.

Time integration relies on a fully implicit backward Euler scheme, with the time interval $\mathcal{I}$ divided into $n_{\Delta t}$ subintervals of length $\Delta t = (t_n - t_{n-1})$. We will use the notation $\Delta x = (x_n - x_{n-1})$ for other time-differenced quantities as well. For the spatial discretization, we introduce the specific spaces

$$\mathcal{Q} := \Big\{ \boldsymbol{v} \mid \boldsymbol{v} \in [C^0(\Omega)]^d, \boldsymbol{v} = \mathbf{0} \text{ on } \Gamma^D_{\mathbf{u}}, \boldsymbol{v}_{|K} \in [\mathbb{Q}_1(K)]^d \ \forall K \in \mathcal{T}^h \Big\}, \tag{10a}$$

$$\mathcal{P} := \Big\{ q \mid q \in L^2(\Omega), q_{|K} \in \mathbb{P}_0(K) \ \forall K \in \mathcal{T}^h \Big\}, \tag{10b}$$

where $C^0(\Omega)$ and $L^2(\Omega)$ are the space of continuous and square Lebesgue-integrable functions on Ω, respectively. $\mathbb{Q}_1(K)$ denotes the space of d-linear functions (trilinear in 3D or bilinear in 2D) and $\mathbb{P}_0(K)$ the space of constant functions on a given element K.

The discrete weak form of Eq. 1 reads: Find $\{\mathbf{u}_n, s_n, p_n\} \in \mathcal{Q} \times \mathcal{P} \times \mathcal{P}$ such that for time step $n = \{1, \ldots, n_{n_{\Delta t}}\}$

$$R_u = \int_\Omega \nabla^s \boldsymbol{v} : \boldsymbol{\sigma}'_n \, \mathrm{d}\Omega - \int_\Omega \nabla \cdot \boldsymbol{v} b p_n \, \mathrm{d}\Omega - \int_\Omega \boldsymbol{v} \cdot \rho_n \mathbf{g} \, \mathrm{d}\Omega - \int_{\Gamma^N_{\mathbf{u}}} \boldsymbol{v} \cdot \bar{\mathbf{t}}_n \, \mathrm{d}\Gamma = 0 \tag{11a}$$

$$R_s = -\int_\Omega \psi \Delta m_w \, \mathrm{d}\Omega + \Delta t \sum_{f \notin \Gamma^N_f} [\![\psi]\!] F^f_{w,n} + \Delta t \int_\Omega \psi q_{w,n} \, \mathrm{d}\Omega = 0 \tag{11b}$$

$$R_p = -\int_\Omega \chi \Delta m_o \, \mathrm{d}\Omega + \Delta t \sum_{f \notin \Gamma^N_f} [\![\chi]\!] F^f_{o,n} + \Delta t \int_\Omega \chi q_{o,n} \, \mathrm{d}\Omega = 0 \tag{11c}$$

for all $\{\boldsymbol{v}, \psi, \chi\} \in \mathcal{Q}, \mathcal{P}, \mathcal{P}$ where $\{\boldsymbol{v}, \psi, \chi\}$ are discrete test functions. The symbol $[\![\cdot]\!]$ denotes the jump of a quantity across face f in $\mathcal{T}^h$. For an internal face, $[\![\chi]\!] = (\chi_{|L} - \chi_{|K})$, with $\chi_{|L}$ and $\chi_{|K}$ the restriction of χ on cells K and L sharing f, respectively. For a face belonging to the domain boundary, the jump expression reduces to $[\![\chi]\!] = -\chi_{|K}$. The term $F^f_{\ell,n}$ denotes a discrete mass flux, i.e., $F^f_{\ell,n} \approx \int_f \boldsymbol{w}_{\ell,n} \cdot \boldsymbol{n}_f \, dA$. These are computed using a standard two-point flux approximation scheme, with upwinding of the phase density and mobility [86]:

$$F^f_{\ell,n} = -\rho^{\mathrm{upw}}_{\ell,n} \lambda^{\mathrm{upw}}_{\ell,n} \Upsilon^f \left([\![p_n]\!] + \rho^f_{\ell,n} g [\![z]\!] \right). \tag{12}$$

Here, Υ^f is the transmissibility coefficient for the face, which is computed knowing the mesh geometry and permeability. The jump in the elevation datum should be understood as the difference in the $z-$coordinate of the respective cell centroids.

The unknown fields are interpolated as

$$\mathbf{u}_n(\mathbf{x}) = \sum_{i=1}^{n_{\mathbf{u}}} \boldsymbol{\eta}_i(\mathbf{x}) u_{i,n}, \tag{13a}$$

$$s_n(\mathbf{x}) = \sum_{j=1}^{n_s} \varphi_j(\mathbf{x}) s_{j,n}, \tag{13b}$$

$$p_n(\mathbf{x}) = \sum_{k=1}^{n_p} \varphi_k(\mathbf{x}) p_{k,n}, \tag{13c}$$

with $\{\boldsymbol{\eta}_i\}$ and $\{\varphi_j\}$ bases for $\mathcal{Q}$ and $\mathcal{P}$, respectively. $\{u_{i,n}\}$ are nodal values of the displacement components, while $\{s_{j,n}\}$ and $\{p_{k,n}\}$ are cell-centered values for the saturation and pressure fields. An identical basis is introduced for the test functions.

The fully discrete system of equations at time t_n is then obtained by introducing these bases into the weak

form (11a)–(11c) and applying the standard finite element procedure. This leads to a set of algebraic equations for the unknown degrees-of-freedom $\{u_{i,n}\}$, $\{s_{j,n}\}$ and $\{p_{k,n}\}$. These degrees-of-freedom are assembled in an algebraic vector $\mathbf{x}_n = \{\mathsf{u}_n, \mathsf{s}_n, \mathsf{p}_n\}$. The nonlinear system of equations is assembled in a residual vector

$$\mathbf{r}_n\ (\mathbf{x}_n, \mathbf{x}_{n-1}) = \begin{bmatrix} \mathsf{r}_n^u \\ \mathsf{r}_n^s \\ \mathsf{r}_n^p \end{bmatrix} = \mathbf{0}. \tag{14}$$

The nonlinearity of the system here results from the nonlinear constitutive behavior embedded in the relative permeability relationship $k_{r\ell}(s)$. Furthermore, this formulation is general enough to accommodate other nonlinear constitutive relationships for the various solid and fluid components. A Newton iteration scheme is used to solve this system, which requires the linearization of the three-field problem. The linearized problem is defined by a Jacobian system with a 3×3 block structure of the form

$$\begin{bmatrix} \mathsf{A}_{uu} & \mathsf{A}_{us} & \mathsf{A}_{up} \\ \mathsf{A}_{su} & \mathsf{A}_{ss} & \mathsf{A}_{sp} \\ \mathsf{A}_{pu} & \mathsf{A}_{ps} & \mathsf{A}_{pp} \end{bmatrix}^k \begin{bmatrix} \delta\mathsf{u} \\ \delta\mathsf{s} \\ \delta\mathsf{p} \end{bmatrix} = - \begin{bmatrix} \mathsf{r}_n^u \\ \mathsf{r}_n^s \\ \mathsf{r}_n^p \end{bmatrix}^k, \tag{15}$$

where $\mathbf{A}^k = \partial \mathbf{r}^k / \partial \mathbf{x}_n$ is the Jacobian matrix, with $\delta\mathsf{u}$, $\delta\mathsf{s}$, and $\delta\mathsf{p}$ the Newton search directions for each field. The superscript k stands for the Newton iteration count. Full expressions for each elemental subvector of $\mathbf{r}$ and submatrix of $\mathbf{A}$ are reported in [38]. We note that the solution of this linear system is typically the most expensive component of a fully implicit code, and good solver performance is therefore essential.

4 Incompressibility

It may not be immediately apparent that the system (15) may be subject to an inf-sup condition on its solvability. Indeed, for many problem configurations the discrete system is perfectly well-posed. Instabilities can arise, however, when two conditions are satisfied:

1. During undrained loading, i.e., as either $\boldsymbol{\kappa} \to 0$ or $\Delta t \to 0$;
2. When the solid and fluid phases approach incompressibility, i.e., $K_s \to \infty$ and $K_\ell \to \infty$ for $\ell = \{w, o\}$.

Note that it is sufficient to merely approach these limits, a situation that occurs frequently in practice. This is particularly true at early simulation times, when small time steps Δt are often required to resolve rapidly evolving solution fields. Liquid and solid compressibilities are also often small for many geologic systems.

To highlight the origin of difficulties, we first revisit the continuum governing equations assuming the conditions above are exactly satisfied. In this case, several relationships simplify, in particular

$$b = 1, \tag{16a}$$
$$\dot{\phi} = \nabla \cdot \dot{\boldsymbol{u}}, \tag{16b}$$
$$\dot{\rho}_s = \dot{\rho}_w = \dot{\rho}_o = 0, \tag{16c}$$
$$\boldsymbol{w}_w = \boldsymbol{w}_o = \mathbf{0}, \tag{16d}$$
$$q_w = q_o = 0. \tag{16e}$$

We set $q_\ell = 0$ here under the assumption that these source terms represent wells, which cannot inject when permeability goes to zero. The mass balance (1b)–(1c) reduces to

$$\frac{\partial}{\partial t}(\phi s) = 0 \tag{17a}$$
$$\frac{\partial}{\partial t}(\phi(1-s)) = 0 \tag{17b}$$

Adding these two equations implies $\dot{\phi} = 0$, and therefore $\dot{s} = 0$. The reduced system of governing equations is therefore

$$\nabla \cdot \boldsymbol{\sigma}' - \nabla p + \rho \mathbf{g} = \mathbf{0} \qquad \text{in } \Omega \times \mathcal{I}, \tag{18a}$$
$$\nabla \cdot \dot{\boldsymbol{u}} = 0 \qquad \text{in } \Omega \times \mathcal{I}, \tag{18b}$$

with $s(\boldsymbol{x}, t) = s_0(\boldsymbol{x})$. We observe that under these conditions the solid deformation field must satisfy a divergence constraint condition, while the saturation field becomes fixed in time at its initial conditions. This result is physically intuitive. If the fluids can neither flow nor compress, they will not allow the solid skeleton to deform volumetrically, nor is there a mechanism for saturations to evolve. The result is a two-field problem only in displacement and pressure. With some additional manipulations one can show that this set of governing equations is equivalent to Stokes' equations.

It is also instructive to perform the same exercise for the algebraic system (15). When phase compressibility is zero and undrained conditions are reached, the Jacobian matrix becomes

$$\mathbf{A}^* = \begin{bmatrix} \mathsf{A}^*_{uu} & & \mathsf{A}^*_{up} \\ \mathsf{A}^*_{su} & \mathsf{A}^*_{ss} & \\ \mathsf{A}^*_{pu} & \mathsf{A}^*_{ps} & \end{bmatrix} \tag{19}$$

with the following expressions for the individual blocks:

$$\left[\mathsf{A}^*_{uu}\right]_{ij} = \int_\Omega \nabla^s \boldsymbol{\eta}^i : \mathbb{C} : \nabla^s \boldsymbol{\eta}^j dV \tag{20a}$$

$$\left[\mathsf{A}^*_{up}\right]_{ij} = -\int_\Omega \nabla \cdot \boldsymbol{\eta}^i \varphi^j dV \tag{20b}$$

$$\left[\mathsf{A}^*_{su}\right]_{ij} = -\rho_w \int_\Omega s_n \varphi^i \nabla \cdot \boldsymbol{\eta}^j dV \tag{20c}$$

$$\left[\mathsf{A}^*_{pu}\right]_{ij} = -\rho_o \int_\Omega (1-s_n) \varphi^i \nabla \cdot \boldsymbol{\eta}^j dV \tag{20d}$$

$$\left[\mathsf{A}^*_{ss}\right]_{ij} = -\rho_w \int_\Omega \phi \varphi^i \varphi^j dV \tag{20e}$$

$$\left[\mathsf{A}^*_{ps}\right]_{ij} = \rho_o \int_\Omega \phi \varphi^i \varphi^j dV \tag{20f}$$

Now imagine that we add the third block row to the second, scaled by their (constant) densities. We observe that

$$\frac{1}{\rho_w}\mathsf{A}^*_{su} + \frac{1}{\rho_o}\mathsf{A}^*_{pu} = \mathsf{A}^{T*}_{up} \tag{21a}$$

$$\frac{1}{\rho_w}\mathsf{A}^*_{ss} + \frac{1}{\rho_o}\mathsf{A}^*_{ps} = \mathsf{0} \tag{21b}$$

We may therefore identify a subsystem for displacements and pressures that is uncoupled from the saturation field,

$$\mathbf{B^*} = \begin{bmatrix} \mathsf{A}^*_{uu} & \mathsf{A}^*_{up} \\ \mathsf{A}^{T*}_{up} & \end{bmatrix} \tag{22}$$

One would arrive at the same system through a direct discretization of the reduced governing equations above. It is clear that this matrix is in saddle-point form, and that the spaces chosen for the pressure and displacement fields must satisfy an inf-sup compatibility condition to ensure $\mathbf{B^*}$ has full rank. For our chosen interpolation, however, this is not the case. As the incompressible limit is approached, $\mathbf{B^*}$—and equivalently, $\mathbf{A^*}$—may contain near-singular modes that can express as spurious oscillations in the pressure field.

5 Stabilized formulation

As a fix for this difficulty, we propose a simple modification to the way the discrete fluxes are treated in Eqs. 11b and 11c. As described earlier, the mesh is decomposed into macroelements. Let Γ_M denote the union of all faces f that lie interior to any macroelement. That is, any two cells connected across a face $f \in \Gamma_M$ are members of the same parent macroelement.

For any face in Γ_M, we augment the physical flux with an additional stabilization flux G^f_ℓ. For a given time increment Δt, we replace

$$\Delta t F^f_{\ell,n} \leftarrow \Delta t F^f_{\ell,n} + G^f_\ell \qquad \forall f \in \Gamma_M \tag{23}$$

where for each phase the stabilization flux is a function of an inter-element jump $[\![\Delta p]\!]$ across the face, scaled by particular constants,

$$G^f_w = -\alpha^f_w [\![\Delta p]\!] \quad \text{with} \quad \alpha^f_w = \tau V^e [\rho_w s]^{\text{upw}}_{n-1}, \tag{24a}$$

$$G^f_o = -\alpha^f_o [\![\Delta p]\!] \quad \text{with} \quad \alpha^f_o = \tau V^e [\rho_o (1-s)]^{\text{upw}}_{n-1} \tag{24b}$$

These artificial fluxes will be used to control spurious pressure modes associated with non-physical pressure jumps across faces. Here, τ is a stabilization parameter and V_e is the volume of the child element in the macroelement. The remaining terms are the upwinded density and phase saturation for the respective phases. Note that these are lagged in time to simplify the linearization, as a lagged approximation of these quantities is usually sufficient for stabilization purposes. We will discuss the choice of stabilization constant below, which is critical to success.

This flux form is quite similar to the physical flux computation (12), so it may be readily added to an existing face-based assembly loop. Any addition of artificial fluxes, however, will break the element-wise mass conservation property of the underlying finite volume scheme. Because these artificial fluxes are only added to internal faces of the macroelement, however, exact mass conservation is still preserved on the macroelement level.

When assembled, these flux terms add additional entries to two blocks of the system matrix,

$$\mathbf{A} = \begin{bmatrix} \mathsf{A}_{uu} & \mathsf{A}_{us} & \mathsf{A}_{up} \\ \mathsf{A}_{su} & \mathsf{A}_{ss} & \mathsf{A}_{sp} + \mathsf{C}_{sp} \\ \mathsf{A}_{pu} & \mathsf{A}_{ps} & \mathsf{A}_{pp} + \mathsf{C}_{pp} \end{bmatrix}, \tag{25}$$

where the stabilizing entries are assembled face-wise for any $f \in \Gamma_M$ as

$$\left[\mathsf{C}_{sp}\right]^f_{ij} = -\alpha^f_w [\![\varphi^i]\!][\![\varphi^j]\!], \tag{26a}$$

$$\left[\mathsf{C}_{pp}\right]^f_{ij} = -\alpha^f_o [\![\varphi^i]\!][\![\varphi^j]\!]. \tag{26b}$$

In the incompressible limit, these contributions will not vanish, so that

$$\mathbf{A^*} = \begin{bmatrix} \mathsf{A}^*_{uu} & & \mathsf{A}^*_{up} \\ \mathsf{A}^*_{su} & \mathsf{A}^*_{ss} & \mathsf{C}_{sp} \\ \mathsf{A}^*_{pu} & \mathsf{A}^*_{ps} & \mathsf{C}_{pp} \end{bmatrix}. \tag{27}$$

In practice, we always solve the three-field problem. However, it is instructive to apply the same reduction procedure as before for the incompressible limit. This leads to a reduced system

$$\mathbf{B^*} = \begin{bmatrix} \mathsf{A}^*_{uu} & \mathsf{A}^*_{up} \\ \mathsf{A}^{T*}_{up} & \mathsf{C} \end{bmatrix} \tag{28}$$

where

$$\mathsf{C} = \frac{1}{\rho_w}\mathsf{C}_{sp} + \frac{1}{\rho_o}\mathsf{C}_{pp}. \tag{29}$$

Thus, the original saddle-point system is modified so that new entries appear in the lower-right-hand block. For each face $f \in \Gamma_M$, this matrix contains contributions

$$[\mathsf{C}]_{ij}^{f} = -\tau V^{e} [\![\varphi^{i}]\!][\![\varphi^{j}]\!]. \tag{30}$$

Because of the macroelement construction, the resulting matrix is extremely sparse. In 3D, it is block-diagonal with one 8×8 block C_M for each macroelement in the mesh, with entries

$$\mathsf{C}_M = -\tau V^{e} \begin{bmatrix} 3 & -1 & & -1 & -1 & & & \\ -1 & 3 & -1 & & & -1 & & \\ & -1 & 3 & -1 & & & -1 & \\ -1 & & -1 & 3 & & & & -1 \\ -1 & & & & 3 & -1 & & -1 \\ & -1 & & & -1 & 3 & -1 & \\ & & -1 & & & -1 & 3 & -1 \\ & & & -1 & -1 & & -1 & 3 \end{bmatrix}, \tag{31}$$

where V^e is the average volume of the child elements in the macroelement. Note that in our mesh geometry, $V^e = A^f d^f$ for any face interior to the macroelement, with A^f the face area and d^f the distance between the centroids of the neighboring cells. By construction, this pattern preserves the underlying two-point flux approximation (TPFA) stencil adopted in the original finite volume scheme, and will not cause any fill-in. Note that the matrices C_{sp} and C_{pp} will have the same sparsity pattern as C, though their entries are weighted by the local saturation and densities at the faces.

For the reduced system, the stabilization contribution C has a very similar form to the local pressure jump (LPJ) stabilization as originally formulated for solving the Stokes equation [65]. Indeed, this basic idea of using inter-element pressure jumps to control spurious modes inspired the method proposed here. There are two key differences for the multiphase poromechanics application, however:

1. In the three-field formulation, a separate contribution is made to each mass balance equation, weighted by appropriate phase density and saturation;
2. The optimal stabilization constant τ will differ due to the nature of the underlying equations.

We still have to address this question of what is an appropriate value for the stabilization parameter τ. As proposed in [76], good candidates for τ can be determined by examining the spectrum of the Schur complement matrix,

$$\mathsf{S} = \mathsf{A}_{up}^{*T} \mathsf{A}_{uu}^{*-1} \mathsf{A}_{up}^{*} - \mathsf{C}, \tag{32}$$

which corresponds to a further block reduction of $\mathbf{B^*}$ to a pressure-only system. We focus on a patch test involving a single macroelement, with rigid and impermeable boundary conditions (Fig. 2). If stability can be demonstrated for a single macroelement, theoretical results in [87, 88] prove

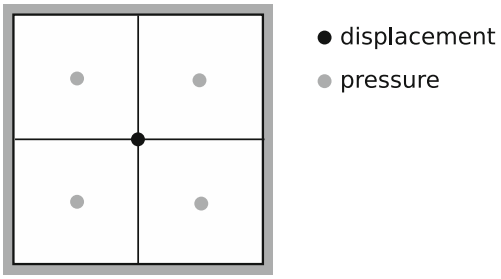

Fig. 2 Single macroelement patch test geometry in 2D, with one pressure in each cell and two displacement components at the central node. The 3D macroelement is similar, involving eight pressures and three displacement components

stability for discretizations on arbitrary grids constructed by "gluing together" stable macroelements.

The resulting Schur complement is rank deficient without stabilization. In 3D, there are eight pressure unknowns in the cells but only three displacement components at the central node. Similar to [77], the eigenvalues and eigenvectors of this system may be readily computed. Let the cells have edge lengths h_x, h_y, and h_z. The element volume is $V = h_x h_y h_z$, and each face has area $A_{xy} = h_x h_y$, $A_{yz} = h_y h_z$, or $A_{xz} = h_x h_z$. The resulting eigenvalues are

$$e_1 = 0 \tag{33a}$$

$$e_2 = e_3 = e_4 = 4V\tau \tag{33b}$$

$$e_5 = 6V\tau \tag{33c}$$

$$e_6 = V\left(2\tau + \frac{9A_{xy}^2}{16\left(A_{xy}^2(\lambda+2G) + A_{xz}^2 G + A_{yz}^2 G\right)}\right) \tag{33d}$$

$$e_7 = V\left(2\tau + \frac{9A_{xz}^2}{16\left(A_{xy}^2 G + A_{xz}^2(\lambda+2G) + A_{yz}^2 G\right)}\right) \tag{33e}$$

$$e_8 = V\left(2\tau + \frac{9A_{yz}^2}{16\left(A_{xy}^2 G + A_{xz}^2 G + A_{yz}^2(\lambda+2G)\right)}\right) \tag{33f}$$

where λ and G are the two Lamé parameters characterizing the elastic mechanical response.

When no stabilization is applied to the macroelement, that is when $\tau = 0$, five out of eight eigenvalues are zero. The null eigenvectors include one constant pressure mode (associated to e_1) and four spurious pressure modes (associated to e_2–e_5). The constant mode is expected here since the boundary conditions only determine the pressure solution up to an arbitrary constant. We see that for $\tau > 0$, the stabilization will remove the spurious pressure modes from the null space of S. Unfortunately, the choice of τ will also impact the physical modes associated with e_6–e_8.

For stability, all eigenvalues must remain bounded away from zero except for the constant mode e_1. Taking τ too large, however, will corrupt the physical solution and

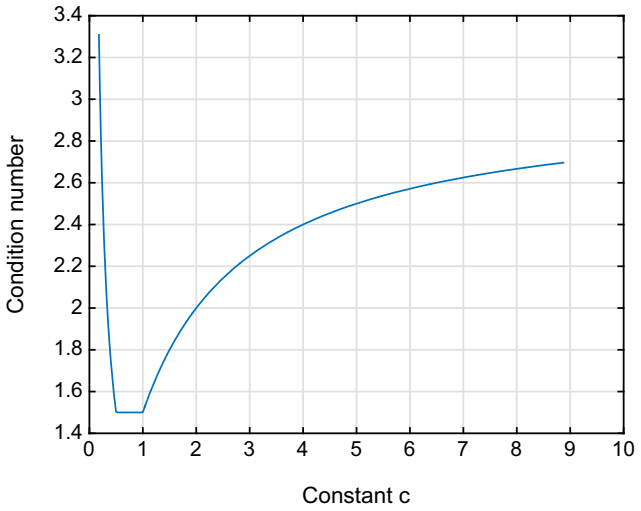

Fig. 3 Analytically computed condition number of S as a function of the stabilization parameter τ for the single macroelement patch test. Here, $c = \tau/\tau^*$ with $c = 1$ being the recommended value

compromise the approximation. A good choice to balance these competing priorities is to choose a τ that minimizes the condition number $\kappa(\mathsf{S}) = e_{\max}/e_{\min}$. Considering a regular cube with equal sides $h_x = h_y = h_z = h$, the minimal condition number is retrieved for any stabilization parameter τ lying within the range

$$\frac{9}{64\,(\lambda + 4G)} \leq \tau \leq \frac{9}{32\,(\lambda + 4G)}. \tag{34}$$

Figure 3 illustrates how the condition number κ varies depending on the stabilization parameter. We can see that the condition number attains its minimal value of $\kappa = 3/2$ within the range prescribed in Eq. 34. Within this range, neither extremal eigenvalue actually depends on τ. Therefore, a reasonable choice for the stabilization parameter is

$$\tau^* = \frac{9}{32\,(\lambda + 4G)}. \tag{35}$$

In order to explore the sensitivity of numerical solutions to this constant, it is convenient to present results in terms of the ratio $c = \tau/\tau^*$, i.e., the ratio of a given stabilization τ to the recommended value τ^*, with $c = 1$ being "optimal."

We emphasize that the recommended value here is based on the analysis of a homogeneous, isotropic macroelement. It therefore only depends on two elastic constants. Depending on the user's needs, a more precise analysis may lead to a stabilization constant that additionally depends on the Biot coefficient, fluid compressibilities, macroelement heterogeneity, and so forth. For example, when $b < 1$ a better estimate is $\tau = b^2\tau^*$. In the case of elasto-plasticity, the mechanical constants should be updated whenever the tangent moduli change. For an anisotropic or highly heterogeneous mechanical model, the appropriate moduli could be taken into account when computing the Schur complement matrix (32). For highly distorted macroelements, the analytical analysis is likely overly demanding and a numerical eigen-decomposition approach may be preferred. The basic roadmap for deriving these more complicated stabilizations, nevertheless, remains the same.

On the other hand, the inclusion of anisotropic permeability or a multi-point flux approximation stencil would have no impact on the proposed stabilization scheme. The purpose of the stabilization is to fix the saddle-point system that arises when $\kappa\Delta t \to 0$. Since we are interested in the limit state when this term vanishes, the structure of the flux discretization makes no difference. Similarly, the inclusion of capillary pressure will impact the overall governing formulation, but the incompressible limit analysis of Section 4 would nearly remain the same. The only difference is that the fluid pressure serving as the Lagrange multiplier in the reduced system would be the effective pressure $\overline{p}$ arising from the chosen multiphase effective stress decomposition. We would arrive at the same stabilization, with the constant only depending on mechanical properties.

In summary, the proposed stabilization method consists of adding the artificial flux terms in Eq. 24 to all macroelement-interior faces, weighted by the stabilization constant recommended in Eq. 35. We remark that for meshes for which a macroelement decomposition is not possible, the proposed stabilization could alternatively be added to *every* internal face in the mesh, mimicking a global pressure jump stabilization technique. This would add stability to the discretization, though the appealing property of exact mass conservation on macroelements would be lost.

6 Numerical examples

We begin with a few single-phase examples ($s = 1$) to demonstrate the performance of the method in a simpler setting. We remark that in the completely undrained limit, the governing equations formally reduce to the Stokes system, and the stabilization technique here exactly mimicks the classic local pressure jump (LPJ) stabilization [65]. We therefore refer the reader to [65] and [77] for additional examples on the efficacy of the LPJ approach for Stokes problems. Below, we instead choose to focus on some classic poromechanical test problems. We conclude the section with a full multiphase demonstration for a benchmark reservoir simulation problem. These numerical experiments were implemented using *Geocentric*, a simulation framework for computational geomechanics that relies heavily on finite element infrastructure from the *deal.ii* library [89].

Table 1 Simulation parameters used in the three single-phase Barry-Mercer examples

Symbol	Parameter	Drained	Undrained	Modified	Units
Δt	Time step	6.14×10^{-5}	10^{-4}	10^{-2}	s
T	Final time	1.54×10^{-3}	10^{-4}	10^{-2}	s
b	Biot coefficient	1	1	1	-
E	Young's modulus	10^5	10^5	2.5	Pa
ν	Poisson ratio	0.1	0.1	0.25	-
k	Permeability	10^{-5}	10^{-9}	10^{-11}	m^2
μ_w	Viscosity	10^{-3}	10^{-3}	10^{-3}	Pa·s
ρ_w	Density	10^3	10^3	10^3	kg/m^3

6.1 Single-phase Examples

For the single-phase examples, we consider several variants of Barry and Mercer's problem for a two-dimensional, poroelastic medium [90]. Parameter values are summarized in Table 1. The first test illustrates that the proposed stabilization scheme does not compromise solution accuracy under drained conditions, when no instabilities are expected. Two subsequent examples confirm the effectiveness of the scheme in suppressing spurious pressure oscillations under undrained conditions.

6.1.1 Drained Barry-Mercer

Barry and Mercer [90] provide an analytical solution for a two-dimensional problem. The problem setup consists of a square domain $\Omega = [0, 1] \times [0, 1]$ subjected to a periodic point source given as

$$q_w(t) = 2\beta\, \delta\,(\mathbf{x} - \mathbf{x}_0)\, \sin(\beta t) \quad \text{with} \quad \beta = (\lambda + 2G)\, \frac{\kappa}{\mu}. \tag{36}$$

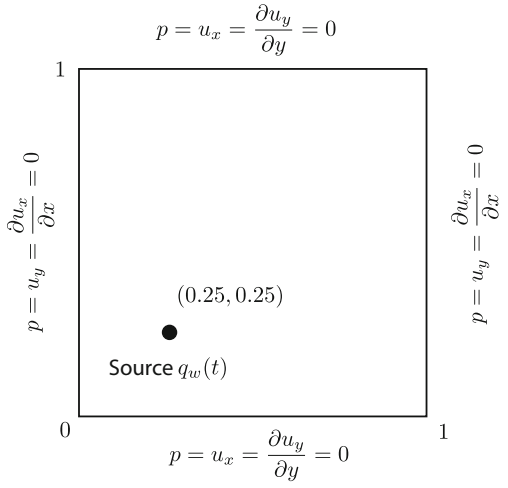

Fig. 4 Geometry and boundary conditions for the Barry-Mercer problem

Here, λ and G denote the two elastic Lamé parameters, while κ and μ are the isotropic absolute permeability and viscosity, respectively. The point source is located at $\mathbf{x}_0 = (0.25, 0.25)$, and $\delta(\cdot)$ indicates a Dirac function. All sides of the computational domain are constrained with zero pressure and zero tangential displacement boundary conditions, as depicted in Fig. 4. The simulation parameters provided in Table 1 (drained conditions) are the same as those used in [42, 50, 91, 92]. Note that the time step and final time correspond to a normalized time $\hat{t} = \beta t$ of $\Delta\hat{t} = 2\pi/100$ and $\hat{t} = \pi/2$, respectively.

Figure 5 shows the resulting pressure profile at the final time along a vertical line through the source point. Both the analytical solution and the numerical solution for different mesh refinements are shown. Good agreement between the exact and computed results is also indicated by Fig. 6, which shows convergence behavior of the L_2-error for the pressure solution for both the stabilized and unstabilized formulations. One observes a linear and essentially identical error behavior for both, indicating that the macroelement

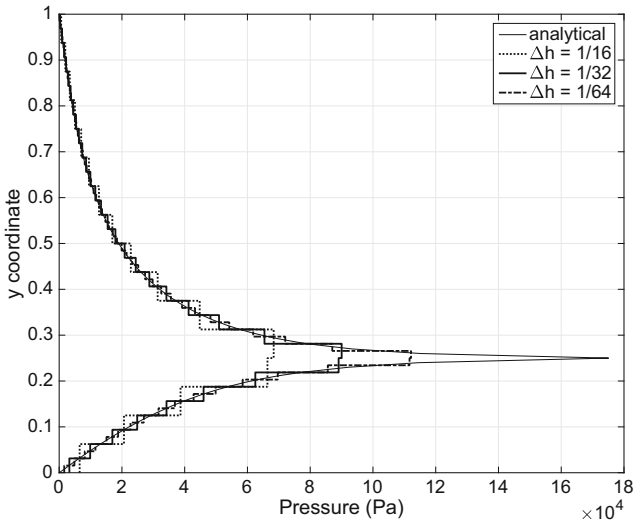

Fig. 5 Pressure plot along the vertical line $x = 0.25$ for the drained Barry-Mercer problem at $\hat{t} = \pi/2$ using the stabilized formulation

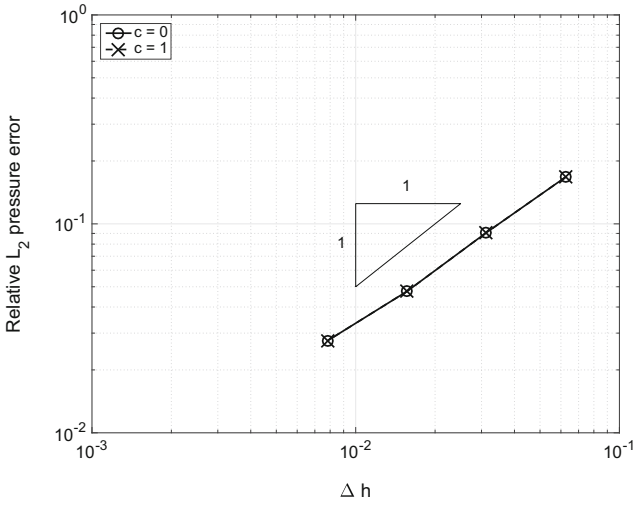

Fig. 6 Convergence of the relative L_2-error in pressure for the drained Barry-Mercer problem at $\hat{t} = \pi/2$, using both the unstabilized ($c = 0$) and stabilized ($c = 1$) formulations

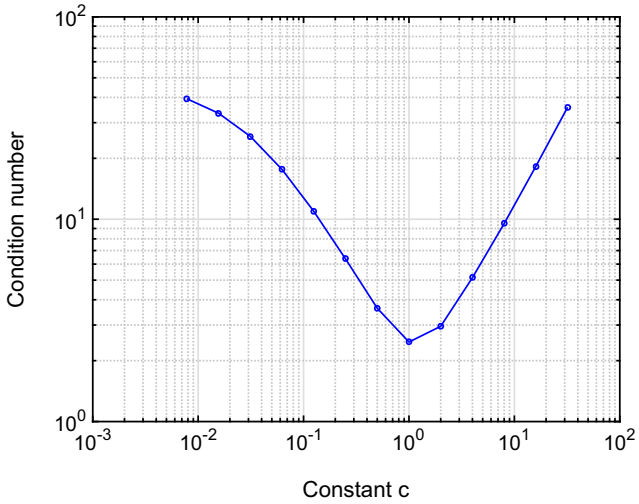

Fig. 8 Computed condition numbers of S' for the undrained Barry-Mercer problem for various stabilization values $\tau = c\tau^*$

stabilization does not compromise solution accuracy in regimes where it is not strictly needed.

6.1.2 Undrained Barry-Mercer

The goal of this example is to show the effectiveness of proposed stabilization scheme in treating non-physical pressure oscillations. These spurious pressure oscillations appear in the limit of low permeability or fast loading rates. As in [50, 91, 92], we use the same simulation parameters as the previous section, but we decrease the value of the permeability to $\kappa = 10^{-9}\,\mathrm{m}^2$ and perform only one time step of $\Delta t = 10^{-4}$ s.

Figure 7 shows the pressure contour plot for the uniformly discretized domain with $\Delta h = 1/16$. The pressure field exhibits mild oscillations close to the source-point. These oscillations are eliminated when using the proposed stabilization technique.

It is also interesting to examine the conditioning of the stabilized system and its impact on iterative solver performance. To do so, we define a scaled Schur-complement matrix,

$$\mathsf{S}' = \mathsf{Q}^{-1}\left(\mathsf{A}_{up}^T\mathsf{A}_{uu}^{-1}\mathsf{A}_{up} - \mathsf{C}\right) \tag{37}$$

where Q is the mass matrix on the pressure space. For the $\mathbb{P}_0$ space, this is a diagonal matrix with entries corresponding to the element volumes. The inverse of this diagonal matrix introduces a volume scaling that allows eigenvalues to be properly compared across different mesh refinement levels.

Figure 8 presents the condition number of the S' for various choices of stabilization constant. The minimum is achieved close to the recommended value τ^* that

Fig. 7 Pressure distribution for the undrained Barry-Mercer problem for the unstabilized (**a**) and stabilized formulation using the stabilization parameter τ with recommended value τ^* (**b**)

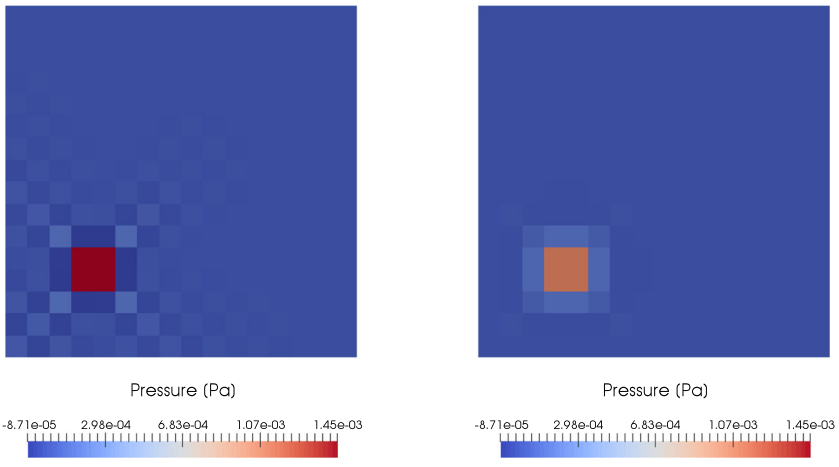

(a) Unstabilized scheme

(b) Stabilized scheme (with $\tau = \tau^*$)

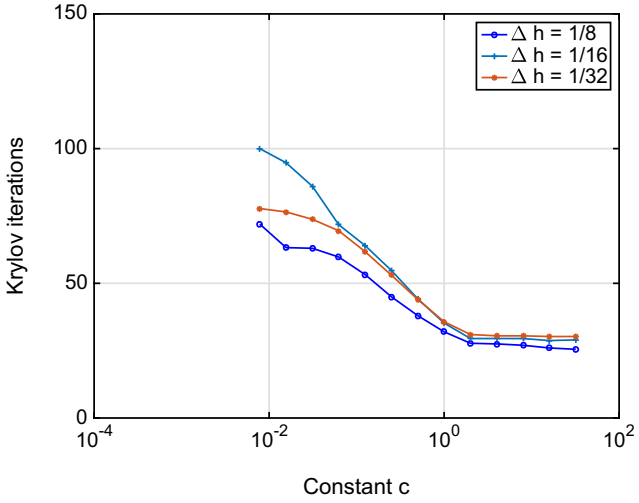

Fig. 9 Krylov iterations to convergence as a function of mesh refinement and stabilization constant $\tau = c\tau^*$ for the undrained Barry-Mercer problem

was inferred from the single macroelement analysis. Furthermore, the removal of near-singular modes from the system matrix has a dramatic impact on the iterative solver performance. Figure 9 presents the number of Krylov iterations to convergence needed for different mesh refinements. For low values of the stabilization constant, the near-singular modes cause a dramatic degradation in the linear solver performance.

6.1.3 Modified undrained Barry-Mercer

This last variant of the Barry-Mercer problem tests the efficacy of the stabilization when even more severe pressure oscillations are present. The setup is based on [45], where the only difference with the previous setup is that the source point is switched from rate-controlled to pressure-controlled. The applied pressure p_s varies according to

$$p_s(t) = p_{\max} \sin(t), \tag{38}$$

with $p_{\max} = 1$. The other simulation parameters follow [45] and are listed in Table 1. An exact solution is not available in this case. However, at early times ($t = 0.01$ s), we can infer that the whole domain should have zero pressure except for the cell where the pressure is enforced. Figure 10 illustrates the solution obtained from the unstabilized and the stabilized scheme for a domain discretized with cell size $\Delta h = 1/16$. To explore the solution sensitivity to the stabilization constant, we present pressure contours for several values of τ smaller and larger than the derived estimate. As expected, the stabilization considering $\tau = \tau^*$ eliminates the wild oscillations, and appears to be the threshold value necessary to do so. At $\tau = 0.1\tau^*$, pervasive oscillations remain. At $\tau = \tau^*$ some very slight oscillations remain near the injector if one looks closely, but overall solution quality is quite good. Taking a larger τ may smooth these last overshoots, but one eventually runs the risk of compromising solution quality with an overly diffusive method.

Table 2 reports the extremal eigenvalues and condition number of the S' for solutions with and without stabilization. One observes that as the mesh is refined the minimal eigenvalue and the condition number converge to an asymptotic value different than zero and infinity, respectively, only when using the stabilized scheme. Figure 11 presents the condition number of the S' matrix as a function of the stabilization constant. Once again, the minimimal condition number is attained when $\tau = \tau^*$. Figure 12 shows the resulting improvement in Krylov convergence.

6.2 Multiphase example

Lastly, we consider a multiphase poromechanics example. The test problem is based on the staircase benchmark problem originally presented in [38]. Figure 13 provides an illustration of the problem geometry. The domain contains two regions, a high-permeability channel and a low-permeability host rock. The high-permeability channel winds its way in a spiral, staircase fashion from an upper injection well to a lower production well. This spiral geometry is obviously artificial, but it introduces very strong coupling between the displacement, pressure, and saturation fields. Water is injected at the upper well, while both fluids may be produced from the lower well. The wells are located in the center of the corner grid blocks and have bottom-hole pressure (BHP) control. The injector (producer) is ramped up to 5 MPa (−5 MPa) overpressure over one day, and then held at a constant pressure. All problem parameters are given in Table 3. We have set the fluids to be incompressible to accentuate any instabilities in the formulation. Specifics regarding the well control, relative permeability model, and mechanical boundary conditions may be found in [38]. At the beginning of the simulation, the initial time step is $\Delta t = 0.0001$ day. This time step is then doubled every step until a maximum time step of $\Delta t = 1$ day is reached. We begin with such a small time step to ensure that the full range of drainage conditions is covered, from undrained to drained. Small time steps are the most problematic from a stability point of view. The whole simulation is run for 100 days.

Figure 14 presents pressure and saturation snapshots for this simulation, using both an unstabilized and stabilized formulation (with $\tau = \tau^*$). At the first time step ($t = 0.0001$ day), checkerboard oscillations are apparent in the pressure field for the unstabilized formulation. Note that we have truncated the colorbar, cutting off the peak pressures, in order to accentuate these oscillations visually. The stabilization successfully suppresses this checkerboarding. At the end of

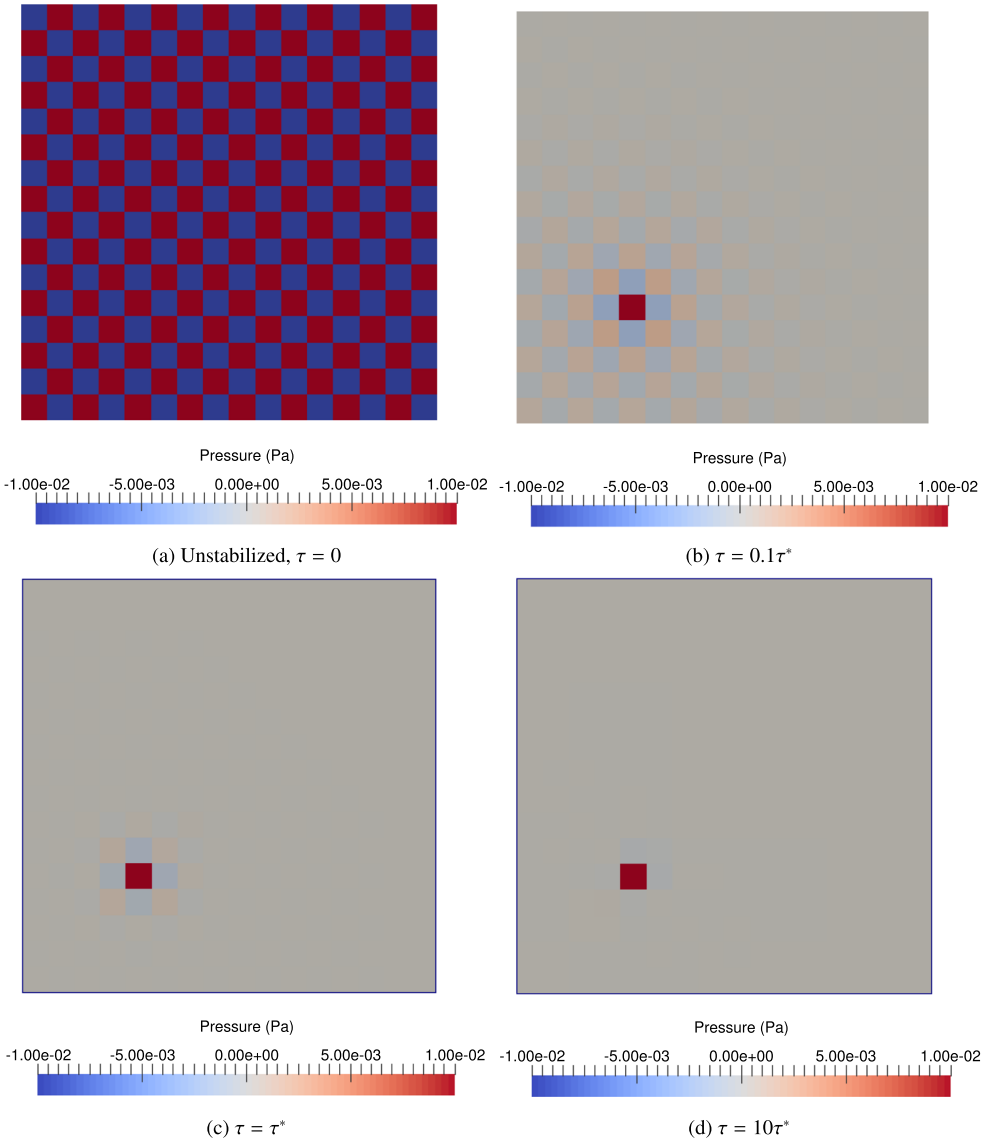

Fig. 10 Pressure distribution for the modified undrained Barry and Mercer's problem, showing solution sensitivity to the stabilization constant τ. We show the results for various stabilization constants, which are proportional to the recommended value τ^*. Here we specifically show the cases where $\tau = 0$ (**a**), $\tau = 0.1\tau^*$ (**b**), $\tau = \tau^*$ (**c**), and $\tau = 10\tau^*$ (**d**)

Table 2 Extremal eigenvalues of the scaled Schur complement matrix for the modified undrained Barry-Mercer problem

Number of cells	$e_{\min}$	$e_{\max}$	Condition number ($e_{\max}/e_{\min}$)
(a) $\tau = 0$			
8×8	2.51 e−03	0.330	131.56
16×16	5.35 e−04	0.333	621.85
32×32	1.19 e−04	0.333	2799.72
(b) $\tau = \tau^*$			
8×8	0.222	0.539	2.421
16×16	0.224	0.546	2.437
32×32	0.225	0.548	2.438

Minimum and maximum eigenvalues as well as the condition number are presented as a function of mesh refinement. Two cases are considered: using (a) an unstabilized scheme and (b) the proposed stabilization

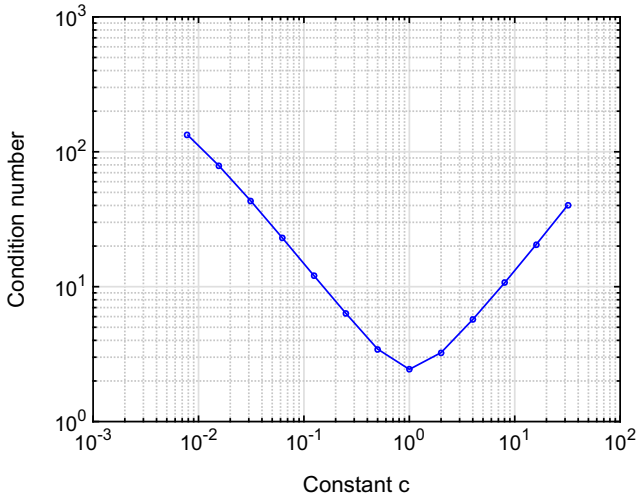

Fig. 11 Computed condition numbers of S' for the modified undrained Barry-Mercer problem for various stabilization values $\tau = c\tau^*$

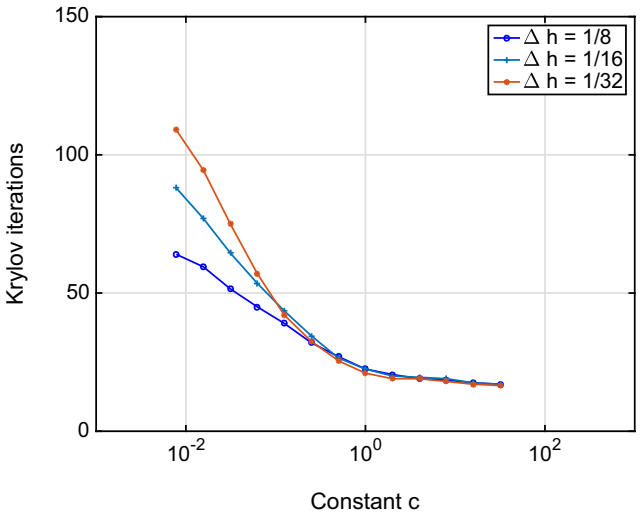

Fig. 12 Krylov iterations as a function of the mesh refinement and the stabilization constant for the modified undrained Barry-Mercer problem

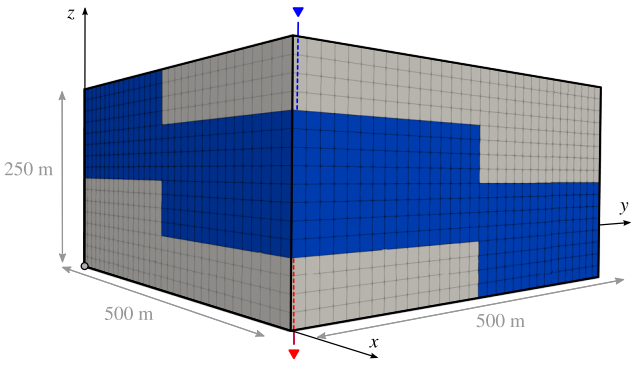

Fig. 13 Problem geometry for the multiphase poromechanics example. Gray region corresponds to a high-permeability channel, which spirals in a "staircase" fashion from the upper injection well (blue triangle) to the lower production well (red triangle). Blue region is a low-permeability zone

Table 3 Simulation parameters used in the multiphase example

Parameter	Units	Value
Porosity:		
High-perm zone	–	0.20
Low-perm zone	–	0.05
Permeability:		
High-perm zone	mD	1000
Low-perm zone	mD	1
Relative perm:		
Residual wetting sat.	–	0.2
Residual non-wetting sat.	–	0.2
Wetting fluid:		
Reference density	kg/m^3	1035
Bulk modulus	MPa	∞
Viscosity	cP	0.3
Non-wetting fluid:		
Reference density	kg/m^3	863
Bulk modulus	MPa	∞
Viscosity	cP	3.0
Rock:		
Young's modulus	MPa	5000
Biot coefficient	–	1
Grain density	kg/m^3	2650
Well control:		
Injection ΔBHP	MPa	5
Production ΔBHP	MPa	-5
Ramp time	Day	1
Well radius	m	0.1524
Skin factor	–	0
Time-stepping:		
Initial Δt	Day	0.0001
Maximum Δt	Day	1
End time	Day	100
Solver tolerances:		
Newton	–	10^{-6}
Krylov	–	10^{-10}

the simulation ($t = 100$ day), we see that the stabilized and unstabilized formulations produce essentially identical results. The addition of the artificial flux terms does not compromise overall solution quality, with the saturation field being advected the same distance along the high-perm channel in both cases.

It is interesting to examine the linear solver behavior at early times in the simulation (Fig. 15). At each Newton step of the nonlinear solver, a preconditioned GMRES iteration is used to solve the Jacobian system. The preconditioner

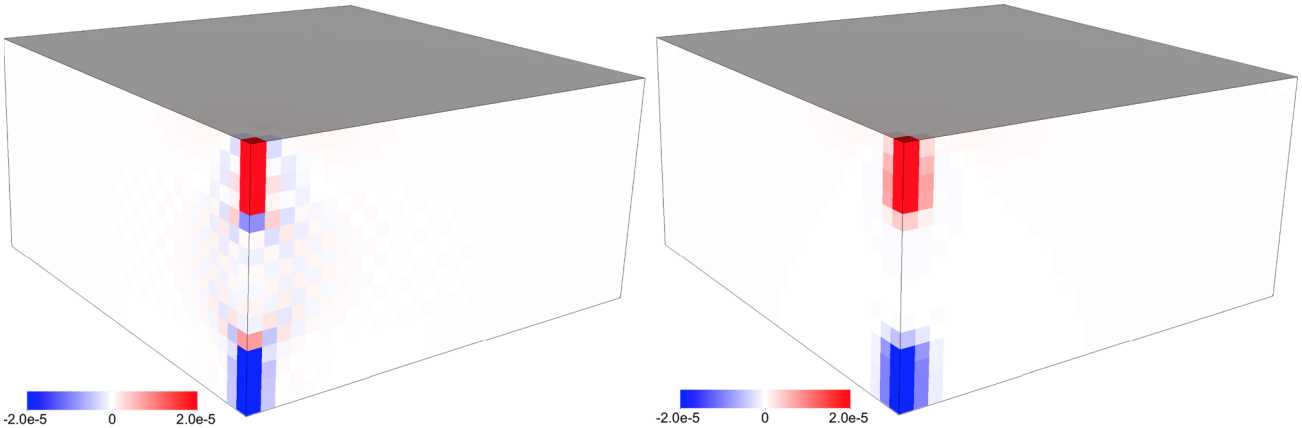

(a) Colorbar is pressure in MPa at $t = 10^{-4}$ day for the unstabilized (left) and stabilized (right) formulations. Note that the colorbar is truncated to visually accentuate oscillations.

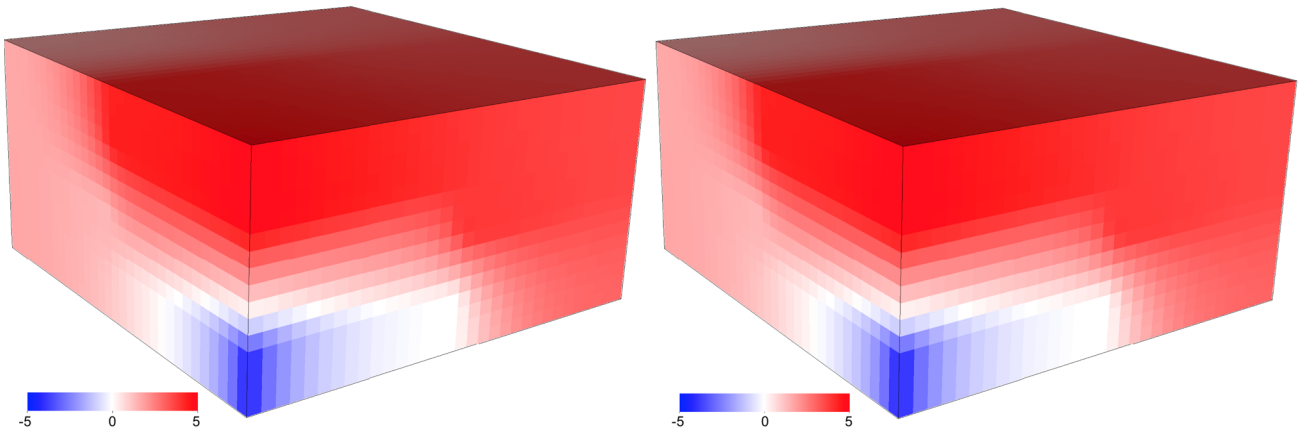

(b) Colorbar is pressure in MPa at $t = 100$ days for the unstabilized (left) and stabilized (right) formulations.

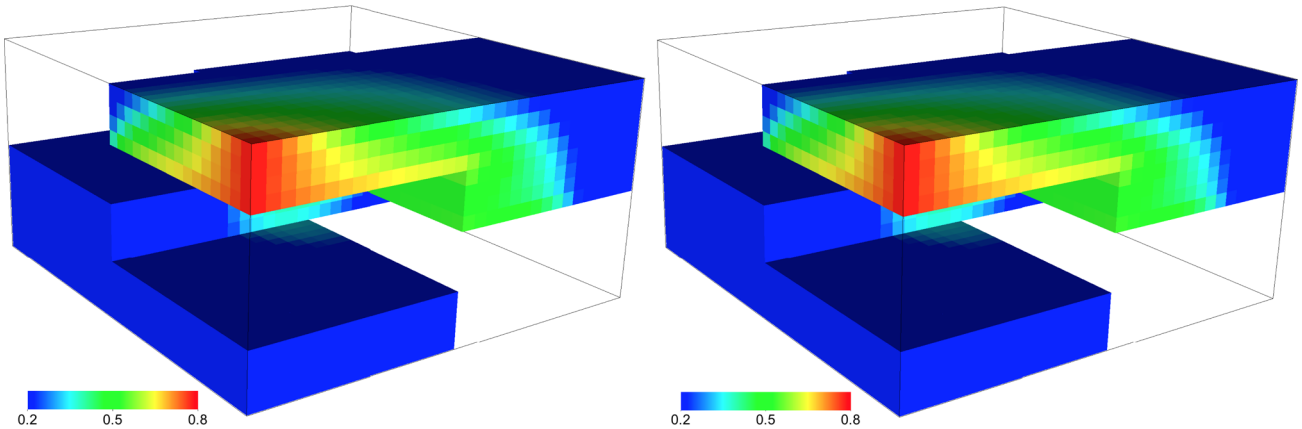

(c) Colorbar is saturation in decimals at $t = 100$ days for the unstabilized (left) and stabilized (right) formulations.

Fig. 14 Comparison of unstabilized and stabilized formulations for the multiphase example. The stabilization suppresses checkerboarding at early simulation times (**a**), but does not otherwise compromise solution quality at late times (**b**, **c**)

we use is the multistage preconditioner described in [38], which in general provides excellent convergence behavior for this class of problem. In the first day of simulation time, however, we see a substantial degradation in solver performance using the unstabilized formulation. This is a direct result of the presence of near-singular modes,

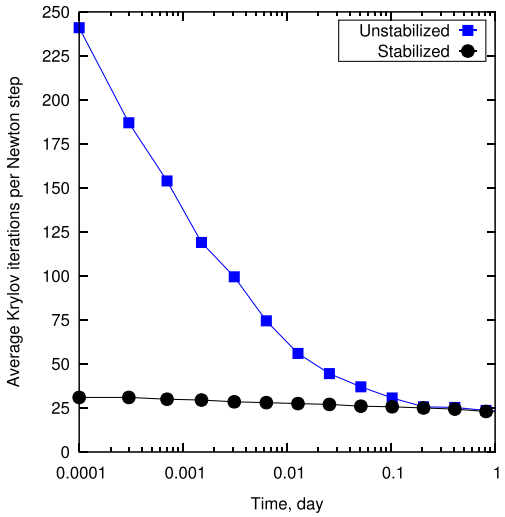

Fig. 15 Comparison of average Krylov iterations per Newton step for the stabilized and unstabilized formulation applied to the multiphase poromechanics example. Without stabilization, the iterative solver convergence degrades at early simulation times when small time steps are employed

to which Krylov-based solvers are extremely sensitive. With the addition of stabilization, however, this problem is completely removed and GMRES once again exhibits excellent convergence. Later in the simulation, as Δt grows, the physical fluxes between elements grow and even the unstabilized formulation becomes intrinsically stable. As a result, we see the solver convergence behavior merge at later times for the two formulations.

7 Conclusion

In this work, we have presented a stabilized formulation for $\mathbb{Q}_1 - \mathbb{P}_0$ discretizations of single- and multiphase poromechanics. The stabilization is achieved by adding artificial flux terms to faces interior to macroelements. We have also identified an appropriate value for the stabilization parameter based on an eigenvalue analysis of an incompressible macroelement patch test. The stabilization is easy to implement in existing codes, and does not change the underlying sparsity pattern of the finite volume stencil. While exact mass conservation on individual elements is sacrificed, exact mass conservation on macroelements is retained. We have demonstrated, through a number of single and multiphase examples, that the method is effective in practice. It can suppress spurious oscillations and also prevent unwanted degradation in iterative solver convergence in the presence of near-singular modes. The latter is a critical issue for large-scale simulations of geosystems.

While the discussion here has been limited to $\mathbb{Q}_1 - \mathbb{P}_0$ discretizations, a similar approach can likely be used for other unstable interpolation pairs involving piecewise-constant pressure approximations—e.g., on more general hexahedral or tetrahedral meshes.

Acknowledgments Funding for JTC and JAW was provided by Total S.A. through the FC-MAELSTROM Project. JTC also acknowledges financial support provided by the Brazilian National Council for Scientific and Technological Development (CNPq) and the John A. Blume Earthquake Engineering Center. RIB was supported by the U.S. Department of Energy, Office of Science, Office of Basic Energy Sciences, Geosciences Research Program, under Award Number DE-FG02-03ER15454 and by the National Science Foundation under Award Numbers CMMI-1462231 and CMMI-1914780. The authors wish to thank Nicola Castelletto for helpful discussions. Portions of this work were performed under the auspices of the U.S. Department of Energy by Lawrence Livermore National Laboratory under Contract DE-AC52-07-NA27344.

References

1. Teatini, P., Ferronato, M., Gambolati, G., Gonella, M.: Groundwater pumping and land subsidence in the Emilia-Romagna coastland, Italy: modeling the past occurrence and the future trend. Water Resources Research 42(1). https://doi.org/10.1029/2005WR004242
2. Borja, R.I., White, J.A.: Continuum deformation and stability analyses of a steep hillside slope under rainfall infiltration. Acta Geotech. **5**(1), 1–14 (2010). https://doi.org/10.1007/s11440-009-0108-1
3. Borja, R.I., Liu, X., White, J.A.: Multiphysics hillslope processes triggering landslides. Acta Geotech. **7**(4), 261–269 (2012). https://doi.org/10.1007/s11440-012-0175-6
4. Camargo, J., Velloso, R.Q., Vargas, E.A.: Numerical limit analysis of three-dimensional slope stability problems in catchment areas. Acta Geotech. **11**(6), 1369–1383 (2016). https://doi.org/10.1007/s11440-016-0459-3
5. Cao, J., Jung, J., Song, X., Bate, B.: On the soil water characteristic curves of poorly graded granular materials in aqueous polymer solutions. Acta Geotech. **13**(1), 103–116 (2018). https://doi.org/10.1007/s11440-017-0568-7
6. Fávero Neto, A.H., Borja, R.I.: Continuum hydrodynamics of dry granular flows employing multiplicative elastoplasticity. Acta Geotech. **13**(5), 1027–1040 (2018). https://doi.org/10.1007/s11440-018-0700-3
7. Ghaffaripour, O., Esgandani, G.A., Khoshghalb, A., Shahbodaghkhan, B.: Fully coupled elastoplastic hydro-mechanical analysis of unsaturated porous media using a meshfree method. International Journal for Numerical and Analytical Methods in Geomechanics. https://doi.org/10.1002/nag.2931
8. Gholami Korzani, M., Galindo-Torres, S.A., Scheuermann, A., Williams, D.J.: SPH approach for simulating hydro-mechanical processes with large deformations and variable permeabilities. Acta Geotech. **13**(2), 303–316 (2018). https://doi.org/10.1007/s11440-017-0610-9
9. Mikaeili, E., Schrefler, B.: XFEM, strong discontinuities and second-order work in shear band modeling of saturated porous media. Acta Geotech. **13**(6), 1249–1264 (2018). https://doi.org/10.1007/s11440-018-0734-6
10. Navas, P., Sanavia, L., López-Querol, S., Yu, R.C.: Explicit meshfree solution for large deformation dynamic problems in saturated porous media. Acta Geotech. **13**(2), 227–242 (2018). https://doi.org/10.1007/s11440-017-0612-7

11. Oka, F., Shahbodagh, B., Kimoto, S.: A computational model for dynamic strain localization in unsaturated elasto-viscoplastic soils. Int. J. Numer. Anal. Methods Geomech. **43**(1), 138–165 (2019). https://doi.org/10.1002/nag.2857
12. Prassetyo, S.H., Gutierrez, M.: High-order ADE scheme for solving the fluid diffusion equation in non-uniform grids and its application in coupled hydro-mechanical simulation. Int. J. Numer. Anal. Methods Geomech. **42**(16), 1976–2000 (2018). https://doi.org/10.1002/nag.2843
13. Song, X., Wang, K., Ye, M.: Localized failure in unsaturated soils under non-isothermal conditions. Acta Geotech. **13**(1), 73–85 (2018). https://doi.org/10.1007/s11440-017-0534-4
14. Wang, M., Feng, Y., Pande, G., Zhao, T.: A coupled 3-dimensional bonded discrete element and lattice Boltzmann method for fluid-solid coupling in cohesive geomaterials. Int. J. Numer. Anal. Methods Geomech. **42**(12), 1405–1424 (2018). https://doi.org/10.1002/nag.2799
15. Wang, W., Zhou, M., Zhang, B., Peng, C.: A dual mortar contact method for porous media and its application to clay-core rockfill dams. Int. J. Numer. Anal. Methods Geomech. **43**(9), 1744–1769 (2019). https://doi.org/10.1002/nag.2930
16. Yan, C., Jiao, Y.-Y., Yang, S.: A 2D coupled hydro-thermal model for the combined finite-discrete element method. Acta Geotech. **14**(2), 403–416 (2019). https://doi.org/10.1007/s11440-018-0653-6
17. Zhou, Z., Du, X., Wang, S., Cai, X., Chen, L.: Micromechanism of the diffusion of cement-based grouts in porous media under two hydraulic operating conditions: constant flow rate and constant pressure. Acta Geotech. **14**(3), 825–841 (2019). https://doi.org/10.1007/s11440-018-0704-z
18. Borja, R.I., Choo, J.: Cam-Clay plasticity, Part VIII: a constitutive framework for porous materials with evolving internal structure. Comput. Methods Appl. Mech. Eng. **309**, 653–679 (2016). https://doi.org/10.1016/j.cma.2016.06.016
19. Borja, R.I., Song, X., Wu, W.: Critical state plasticity. Part VII: triggering a shear band in variably saturated porous media. Comput. Methods Appl. Mech. Eng. **261-262**, 66–82 (2013). https://doi.org/10.1016/j.cma.2013.03.008
20. Borja, R.I., Yin, Q., Zhao, Y.: Cam-Clay plasticity. Part IX: on the anisotropy, heterogeneity, and viscoplasticity of shale. Comput. Methods Appl. Mech. Eng. **360**, 112695 (2020). https://doi.org/10.1016/j.cma.2019.112695
21. Zoback, M.D.: Reservoir Geomechanics. Cambridge University Press. https://doi.org/10.1017/CBO9780511586477 (2007)
22. Feng, Y., Gray, K.E.: XFEM-based cohesive zone approach for modeling near-wellbore hydraulic fracture complexity. Acta Geotech. **14**(2), 377–402 (2019). https://doi.org/10.1007/s11440-018-0645-6
23. Mashhadian, M., Abedi, S., Noshadravan, A.: Probabilistic multiscale characterization and modeling of organic-rich shale poroelastic properties. Acta Geotech. **13**(4), 781–800 (2018). https://doi.org/10.1007/s11440-018-0652-7
24. Peng, S., Zhang, Z., Mou, J., Zhao, B., Liu, Z., Wang, J.: Fully coupled hydraulic fracture simulation using the improved element partition method. Int. J. Numer. Anal. Methods Geomech. **43**(1), 441–460 (2019). https://doi.org/10.1002/nag.2870
25. Semnani, S.J., White, J.A., Borja, R.I.: Thermoplasticity and strain localization in transversely isotropic materials based on anisotropic critical state plasticity. Int. J. Numer. Anal. Methods Geomech. **40**(18), 2423–2449 (2016). https://doi.org/10.1002/nag.2536
26. Shiozawa, S., Lee, S., Wheeler, M.F.: The effect of stress boundary conditions on fluid-driven fracture propagation in porous media using a phase-field modeling approach. Int. J. Numer. Anal. Methods Geomech. **43**(6), 1316–1340 (2019). https://doi.org/10.1002/nag.2899
27. Yan, C., Jiao, Y.-Y.: FDEM-TH3D: a three-dimensional coupled hydrothermal model for fractured rock. Int. J. Numer. Anal. Methods Geomech. **43**(1), 415–440 (2019). https://doi.org/10.1002/nag.2869
28. Zhang, Q., Choo, J., Borja, R.I.: On the preferential flow patterns induced by transverse isotropy and non-Darcy flow in double porosity media. Comput. Methods Appl. Mech. Eng. **353**, 570–592 (2019). https://doi.org/10.1016/j.cma.2019.04.037
29. Zhao, Y., Semnani, S.J., Yin, Q., Borja, R.I.: On the strength of transversely isotropic rocks. Int. J. Numer. Anal. Methods Geomech. **42**(16), 1917–1934 (2018). https://doi.org/10.1002/nag.2809
30. Zhao, Y., Borja, R.I.: Deformation and strength of transversely isotropic rocks. In: Wu, W. (ed.) Desiderata Geotechnica, Springer International Publishing, pp. 237–241, Cham (2019). https://doi.org/10.1007/978-3-030-14987-1_28
31. Verdon, J.P., Kendall, J.-M., Stork, A.L., Chadwick, R.A., White, D.J., Bissell, R.C.: Comparison of geomechanical deformation induced by megatonne-scale CO2 storage at Sleipner, Weyburn, and In Salah. Proc. Natl. Acad. Sci. **110**(30), E2762–E2771 (2013). https://doi.org/10.1073/pnas.1302156110
32. White, J.A., Chiaramonte, L., Ezzedine, S., Foxall, W., Hao, Y., Ramirez, A., McNab, W.: Geomechanical behavior of the reservoir and caprock system at the In Salah CO2 storage project. Proc. Natl. Acad. Sci. **111**(24), 8747–8752 (2014). https://doi.org/10.1073/pnas.1316465111
33. Jin, W., Arson, C.: Fluid-driven transition from damage to fracture in anisotropic porous media: a multi-scale XFEM approach, Acta Geotechnica. https://doi.org/10.1007/s11440-019-00813-x
34. de Boer, R.: Theory of porous media: highlights in historical development and current state. Springer Science & Business Media. https://doi.org/10.1007/978-3-642-59637-7 (2012)
35. Coussy, O.: Poromechanics. Wiley, New York. https://doi.org/10.1002/0470092718 (2005)
36. Biot, M.A.: General theory of three-dimensional consolidation. J. Appl. Phys. **12**(2), 155–164 (1941). https://doi.org/10.1063/1.1712886
37. White, J.A., Castelletto, N., Tchelepi, H.A.: Block-partitioned solvers for coupled poromechanics: a unified framework. Comput. Methods Appl. Mech. Eng. **303**, 55–74 (2016). https://doi.org/10.1016/j.cma.2016.01.008
38. White, J.A., Castelletto, N., Klevtsov, S., Bui, Q.M., Osei-Kuffuor, D., Tchelepi, H.A.: A two-stage preconditioner for multiphase poromechanics in reservoir simulation. Comput Methods Appl. Mech. Eng. **357**:112575. https://doi.org/10.1016/j.cma.2019.112575 (2019)
39. Murad, M.A., Loula, A.F.D.: On stability and convergence of finite element approximations of Biot's consolidation problem. Int. J. Numer. Methods Eng. **37**(4), 645–667 (1994). https://doi.org/10.1002/nme.1620370407
40. Settari, A., Mourits, F.M.: A coupled reservoir and geomechanical simulation system. SPE J. **3**(03), 219–226 (1998). https://doi.org/10.2118/50939-PA
41. Jha, B., Juanes, R.: A locally conservative finite element framework for the simulation of coupled flow and reservoir geomechanics. Acta Geotech. **2**(3), 139–153 (2007). https://doi.org/10.1007/s11440-007-0033-0
42. Phillips, P.J., Wheeler, M.F.: A coupling of mixed and continuous Galerkin finite element methods for poroelasticity II: the discrete-in-time case. Comput. Geosci. **11**(2), 145–158 (2007). https://doi.org/10.1007/s10596-007-9044-z
43. Ferronato, M., Castelletto, N., Gambolati, G.: A fully coupled 3-D mixed finite element model of biot consolidation. J. Comput. Phys. **229**(12), 4813–4830. https://doi.org/10.1016/j.jcp.2010.03.018 (2010)

44. Kim, J., Tchelepi, H.A., Juanes, R.: Stability, accuracy, and efficiency of sequential methods for coupled flow and geomechanics. SPE J. **16**(02), 249–262 (2011). https://doi.org/10.2118/119084-PA
45. Haga, J.B., Osnes, H., Langtangen, H.P.: On the causes of pressure oscillations in low-permeable and low-compressible porous media. Int. J. Numer. Anal. Methods Geomech. **36**(12), 1507–1522 (2012). https://doi.org/10.1002/nag.1062
46. Prévost, J.H.: Two-way coupling in reservoir geomechanical models: vertex-centered Galerkin geomechanical model cell-centered and vertex-centered finite volume reservoir models. Int. J. Numer. Methods Eng. **98**(8), 612–624 (2014). https://doi.org/10.1002/nme.4657
47. Castelletto, N., White, J.A., Tchelepi, H.A.: Accuracy and convergence properties of the fixed-stress iterative solution of two-way coupled poromechanics. Int. J. Numer. Anal. Methods Geomech. **39**(14), 1593–1618 (2015). https://doi.org/10.1002/nag.2400
48. Nordbotten, J.M.: Cell-centered finite volume discretizations for deformable porous media. Int. J. Numer. Methods Eng. **100**(6), 399–418 (2014). https://doi.org/10.1002/nme.4734
49. Nordbotten, J.M.: Stable cell-centered finite volume discretization for Biot equations. SIAM J. Numer. Anal. **54**(2), 942–968 (2016). https://doi.org/10.1137/15M1014280
50. Rodrigo, C., Gaspar, F., Hu, X., Zikatanov, L.: Stability and monotonicity for some discretizations of the Biot's consolidation model. Comput. Methods Appl. Mech. Eng. **298**, 183–204 (2016). https://doi.org/10.1016/j.cma.2015.09.019
51. Hu, X., Rodrigo, C., Gaspar, F.J., Zikatanov, L.T.: A nonconforming finite element method for the Biot's consolidation model in poroelasticity. J. Comput. Appl. Math. **310**, 143–154 (2017). https://doi.org/j.cam.2016.06.003
52. Honório, H.T., Maliska, C.R., Ferronato, M., Janna, C.: A stabilized element-based finite volume method for poroelastic problems. J. Comput. Phys. **364**, 49–72. https://doi.org/10.1016/j.jcp.2018.03.010 (2018)
53. Choo, J., Lee, S.: Enriched Galerkin finite elements for coupled poromechanics with local mass conservation. Comput. Methods Appl. Mech. Eng. **341**, 311–332 (2018). https://doi.org/10.1016/j.cma.2018.06.022
54. Sokolova, I., Bastisya, M.G., Hajibeygi, H.: Multiscale finite volume method for finite-volume-based simulation of poroelasticity. J. Comput. Phys. **379**:309–324. https://doi.org/10.1016/j.jcp.2018.11.039 (2019)
55. Liu, F., Borja, R.I.: Stabilized low-order finite elements for frictional contact with the extended finite element method. Compute. Methods Appl. Mech. Eng. **199**(37), 2456–2471. https://doi.org/10.1016/j.cma.2010.03.030 (2010)
56. Babuška, I.: The finite element method with Lagrangian multipliers. Numer. Math. **20**(3), 179–192 (1973). https://doi.org/10.1007/BF01436561
57. Brezzi, F.: On the existence, uniqueness and approximation of saddle-point problems arising from Lagrangian multipliers. R.A.I.R.O Anal. Numér. **8**(R2), 129–151 (1974). https://doi.org/10.1051/m2an/197408R201291
58. Brezzi, F., Pitkäranta, J.: On the Stabilization of Finite Element Approximations of the Stokes Equations, Vieweg+Teubner Verlag, pp. 11–19. https://doi.org/10.1007/978-3-663-14169-3_2 (1984)
59. Hughes, T.J., Franca, L.P., Balestra, M.: A new finite element formulation for computational fluid dynamics: V. Circumventing the Babuška-Brezzi condition: a stable Petrov-Galerkin formulation of the Stokes problem accommodating equal-order interpolations. Comput. Methods Appl. Mech. Eng. **59**(1), 85–99. https://doi.org/10.1016/0045-7825(86)90025-3 (1986)
60. Dohrmann, C.R., Bochev, P.B.: A stabilized finite element method for the Stokes problem based on polynomial pressure projections. Int. J. Numer. Methods Fluids **46**(2), 183–201 (2004). https://doi.org/10.1002/fld.752
61. Fortin, M., Boivin, S.: Iterative stabilization of the bilinear velocity–constant pressure element. Int. J. Numer. Methods Fluids **10**(2), 125–140 (1990). https://doi.org/10.1002/fld.1650100202
62. Bochev, P., Dohrmann, C., Gunzburger, M.: Stabilization of low-order mixed finite elements for the Stokes equations. SIAM J. Numer. Anal. **44**(1), 82–101 (2006). https://doi.org/10.1137/S0036142905444482
63. Burman, E., Hansbo, P.: A unified stabilized method for Stokes and Darcy's equations. J. Comput. Appl. Math. **198**(1), 35–51. https://doi.org/10.1016/j.cam.2005.11.022 (2007)
64. Hughes, T.J., Franca, L.P.: A new finite element formulation for computational fluid dynamics: VII. The Stokes problem with various well-posed boundary conditions: symmetric formulations that converge for all velocity/pressure spaces, Comput. Methods Appl. Mech. Eng. **65**(1), 85–96. https://doi.org/10.1016/0045-7825(87)90184-8 (1987)
65. Silvester, D., Kechkar, N.: Stabilised bilinear-constant velocity-pressure finite elements for the conjugate gradient solution of the Stokes problem. Comput. Methods Appl. Mech. Eng. **79**(1), 71–86. https://doi.org/10.1016/0045-7825(90)90095-4 (1990)
66. Pitkäranta, J., Saarinen, T.: A multigrid version of a simple finite element method for the Stokes problem. Math. Comput. **45**(171), 1–14 (1985)
67. Aguilar, G., Gaspar, F., Lisbona, F., Rodrigo, C.: Numerical stabilization of Biot's consolidation model by a perturbation on the flow equation. Int. J. Numer. Methods Eng. **75**(11), 1282–1300 (2008). https://doi.org/10.1002/nme.2295
68. White, J.A., Borja, R.I.: Stabilized low-order finite elements for coupled solid-deformation/fluid-diffusion and their application to fault zone transients. Comput. Methods Appl. Mech. Eng. **197**(49), 4353–4366. https://doi.org/10.1016/j.cma.2008.05.015 (2008)
69. Preisig, M., Prévost, J.H.: Stabilization procedures in coupled poromechanics problems: a critical assessment. Int. J. Numer. Anal. Methods Geomech. **35**(11), 1207–1225 (2011). https://doi.org/10.1002/nag.951
70. Choo, J., Borja, R.I.: Stabilized mixed finite elements for deformable porous media with double porosity. Comput. Methods Appl. Mech. Eng. **29**(3), 131–154 (2015). https://doi.org/10.1016/j.cma.2015.03.023
71. Sun, W., Ostien, J.T., Salinger, A.G.: A stabilized assumed deformation gradient finite element formulation for strongly coupled poromechanical simulations at finite strain. Int. J. Numer. Anal. Methods Geomech. **37**(16), 2755–2788 (2013). https://doi.org/10.1002/nag.2161
72. Berger, L., Bordas, R., Kay, D., Tavener, S.: Stabilized lowest-order finite element approximation for linear three-field poroelasticity. SIAM J. Sci. Comput. **37**(5), A2222–A2245 (2015). https://doi.org/10.1137/15M1009822
73. Rodrigo, C., Hu, X., Ohm, P., Adler, J.H., Gaspar, F.J., Zikatanov, L.: New stabilized discretizations for poroelasticity and the Stokes' equations. Comput. Methods Appl. Mech. Eng. **341**, 467–484 (2018). https://doi.org/10.1016/j.cma.2018.07.003
74. Wan, J.: Stabilized Finite Element Methods for Coupled Geomechanics and Multiphase Flow. Ph.D. thesis, Stanford University (2002)
75. Truty, A., Zimmermann, T.: Stabilized mixed finite element formulations for materially nonlinear partially saturated two-phase media. Comput. Methods Appl. Mech. Eng. **195**(13), 1517–1546. https://doi.org/10.1016/j.cma.2005.05.044 (2006)
76. Silvester, D.: Optimal low order finite element methods for incompressible flow. Comput. Methods Appl. Mech. Eng. **111**(3-4), 357–368 (1994). https://doi.org/10.1016/0045-7825(94)90139-2

77. Elman, H.C., Silvester, D.J., Wathen, A.J.: Finite elements and fast iterative solvers: with applications in incompressible fluid dynamics. Oxford University Press (2005)
78. Tchonkova, M., Peters, J., Sture, S.: A new mixed finite element method for poro-elasticity. Int. J. Numer. Anal. Methods Geomech. **32**(6), 579–606 (2008). https://doi.org/10.1002/nag.630
79. Gaspar, F.J., Rodrigo, C.: On the fixed-stress split scheme as smoother in multigrid methods for coupling flow and geomechanics. Comput. Methods Appl. Mech. Eng. **326**, 526–540 (2017). https://doi.org/10.1016/j.cma.2017.08.025
80. Bui, Q.M., Osei-Kuffuor, D., Castelletto, N., White, J.A.: A scalable multigrid reduction framework for multiphase poromechanics of heterogeneous media, arXiv:1904.05960
81. Ertekin, T., Abou-Kassem, J.H., King, G.R.: Basic Applied Reservoir Simulation. Society of Petroleum Engineers, Richardson (2001)
82. Peaceman, D.W.: Interpretation of well-block pressures in numerical reservoir simulation. Soc. Pet. Eng. AIME J. **18**(3), 183–194 (1978). https://doi.org/10.2118/6893-PA
83. Chen, Z., Huan, G., Ma, Y.: Computational Methods for Multiphase Flows in Porous. Society for Industrial and Applied Mathematics, Philadelphia (2006)
84. Qin, J., Zhang, S.: On the selective local stabilization of the mixed Q1–P0 element. Int. J. Numer. Methods Fluids **55**(12), 1121–1141 (2007). https://doi.org/10.1002/fld.1505
85. Griffiths, D., Silvester, D.: Unstable modes of the Q1–P0 element, Technical Report NA - 257
86. Aziz, K.: Petroleum Reservoir Simulation, vol. 476. Applied Science Publishers, London (1979)
87. Boland, J.M., Nicolaides, R.A.: Stability of finite elements under divergence constraints. SIAM J. Numer. Anal. **20**(4), 722–731 (1983). https://doi.org/10.1137/0720048
88. Stenberg, R.: Analysis of mixed finite element methods for the Stokes problem: a unified approach. Math. Comput. **42**(165), 9–23 (1984). https://doi.org/10.2307/2007557
89. Bangerth, W., Hartmann, R., Kanschat, G.: deal.II – a General Purpose Object Oriented Finite Element Library, ACM Trans. Math. Softw. **33**(4), 24/1–24/27 (2007)
90. Barry, S., Mercer, G.: Exact solutions for two-dimensional time-dependent flow and deformation within a poroelastic medium. J. Appl. Mech. **66**(2), 536–540 (1999). https://doi.org/10.1115/1.2791080
91. Fu, G.: A high-order HDG method for the Biot's consolidation model. Comput. Math. Appl. **77**(1), 237–252. https://doi.org/10.1016/j.camwa.2018.09.029 (2019)
92. Boffi, D., Botti, M., Di Pietro, D.A.: A nonconforming high-order method for the Biot problem on general meshes. SIAM J. Sci. Comput. **38**(3), A1508–A1537 (2016). https://doi.org/10.1137/15M1025505